

Radiation-Assisted Formation of Metal Nanoparticles in Molten Salts

Elaine T. Dias, Simerjeet K. Gill,* Yang Liu, Phillip Halstenberg, Sheng Dai, Jiahao Huang, Julia Mausz, Ruchi Gakhar, William C. Phillips, Shannon Mahurin, Simon M. Pimblott, James F. Wishart, and Anatoly I. Frenkel*



Cite This: *J. Phys. Chem. Lett.* 2021, 12, 157–164



Read Online

ACCESS |



Metrics & More

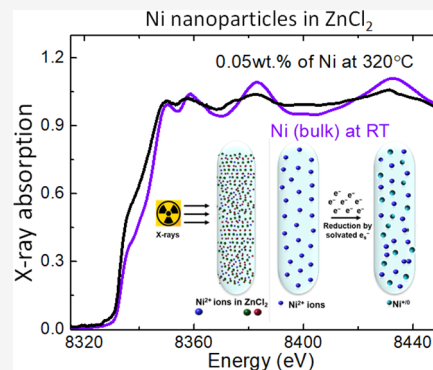


Article Recommendations



Supporting Information

ABSTRACT: Knowledge of structural and thermal properties of molten salts is crucial for understanding and predicting their stability in many applications such as thermal energy storage and nuclear energy systems. Probing the behavior of metal contaminants in molten salts is presently limited to either foreign ionic species or metal nanocrystals added to the melt. To bridge the gap between these two end states and follow the nucleation and growth of metal species in molten salt environment *in situ*, we use synchrotron X-rays as both a source of solvated electrons for reducing Ni^{2+} ions added to ZnCl_2 melt and as an atomic-level probe for detecting formation of zerovalent Ni nanoparticles. By combining extended X-ray absorption fine structure analysis with X-ray absorption near edge structure modeling, we obtained the average size and structure of the nanoparticles and proposed a radiation-induced reduction mechanism of metal ions in molten salts.



The high thermal conductivity and relatively low melting point of molten salts are the main reasons why they make excellent candidate materials for thermal energy storage and heat transfer media for solar and nuclear energy applications.¹ However, a major challenge to their utilization is the strong corrosive effect of molten salt media on metallic alloys, which limits the satisfactory performance of containers and structural materials. Notably, molten salts in nuclear fission reactors face a complex environment with coupled extremes of high temperature and radiation, as well as compositional change over time resulting from in-growth of fission products and the dissolution of corrosion products. Fundamental understanding of molten salt properties requires elucidating how metal speciation evolves in both high temperature and ionizing radiation environments with advanced characterization methods to probe the factors that control metal ion solubility and chemistry.

Exposure of a molten salt to an electromagnetic,^{2,3} energetic electrons,^{4,5} or ion⁶ irradiation source produce solvated electrons. Solvated electrons are highly reactive transient species that reduce metal ions and ultimately may cause the formation of agglomerated structures, such as metal nanoparticles, that are not spontaneously formed in unirradiated molten salts except by powerful reducing agents^{2,7} or reduction methods such as electrochemical deposition⁸ or plasma electrochemistry.⁹ These ligand-free nanoparticles may form a colloidal solution changing the physical and chemical properties of the medium, increasing the thermal conductivity of the molten salt systems, and thus affecting its performance for heat transfer and thermal storage.^{10–12} Therefore, for comprehensive understanding of the behavior of metal ions

and metallic nanoparticles in molten salts, understanding the interplay between their redox chemistry and their solubility (or segregation) is required.

In a previous study, we investigated the interactions of Ni^{2+} and Co^{2+} solutes in molten ZnCl_2 for a range of conditions spanning across their solubility limits using spectroscopic methods.¹³ A combination of *in situ* X-ray absorption fine structure (XAFS) and optical spectroscopies, assisted by *ab initio* molecular dynamics simulations, revealed a variety of local coordination environments ranging from tetrahedral to square pyramidal to octahedral as well as their mixtures depending on the solute ion, its concentration and the salt temperature.¹³ That study focused only on the divalent ionic forms of Ni and Co, with the metal ions coordinated by four or more Cl^- ions at all temperatures and concentrations, and on the both sides of the solubility limit in the case of NiCl_2 .

Here, we study the formation of nickel nanoparticles in ZnCl_2 molten salt environment via X-ray-induced reduction. Synchrotron-based X-ray radiation with tunable energy is an attractive choice as it can, on one hand, initiate the reduction of metal ions and, on the other hand, probe the local structure of metal nanoparticles that may form as a result. Extended X-ray absorption fine structure (EXAFS) and X-ray absorption

Received: October 26, 2020

Accepted: December 3, 2020

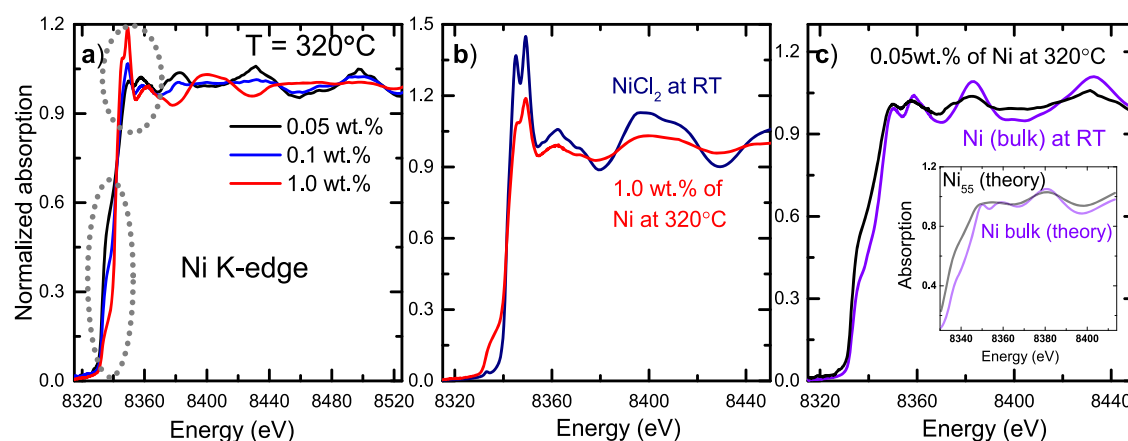


Figure 1. Normalized absorption coefficients at the Ni K-edge for (a) 0.05, 0.1, and 1.0 wt % NiCl₂ in ZnCl₂ at 320 °C, (b) 1.0 wt % NiCl₂ in ZnCl₂ at 320 °C with pure NiCl₂ at RT shown as a reference, and (c) 0.05 wt % NiCl₂ in ZnCl₂ at 320 °C with Ni metal foil a reference. The inset in part c shows simulated XANES spectra for bulk Ni metal and 55-atom Ni nanoparticles using FEFF9 code.

near-edge structure (XANES) are element-specific techniques that can interrogate the local environment of metal species in molten salts under high-temperature conditions.^{13–17} EXAFS probes short-range structural order and provides direct information on coordination number, interatomic distance and amount of disorder, while XANES gives the chemical structure and oxidation states in the local environment of the absorber. A recent work reported an XAFS study of [BMIM][AuCl₄] ionic liquid in which the formation of Au–Au bonds was facilitated by solvated electrons generated as a result of X-ray irradiation.¹⁸ With their strong reducing capacity, the solvated electrons reduce the Au³⁺ cation first to a low-valence (Au²⁺/Au⁺) state before ultimately reducing it to the zerovalent metallic state. While several examples of X-ray induced nanoparticle formation in aqueous solutions^{19,20} and ionic liquids are known,^{21,22} there are no reports, to the best of our knowledge, of X-ray-assisted production of zerovalent metals in molten salts.

In this work, we report the application of *in situ* XAS studies to investigate the X-ray induced formation of Ni nanoparticles in 0.05–1.0 wt % Ni²⁺ in molten ZnCl₂. While at room temperature only Ni²⁺ was observed for all concentrations, at 320 °C (i.e., above the melting point of ZnCl₂) we observed and quantified a variety of Ni redox species varying from Ni⁰ to Ni²⁺ with the relative amounts depending on the relationship between the amount of Ni²⁺ ions in the precursor solution and the radiation dose. In our analysis, we combine first-principles XANES modeling and neural network-assisted data processing with EXAFS fitting methods to elucidate the structure and the size of the Ni nanoparticles formed in molten ZnCl₂ at 320 °C.

NiCl₂ powder (99.99% purity, trace metals basis) and ZnCl₂ (99.999%, anhydrous) were purchased from Sigma-Aldrich. The ZnCl₂ was purified by distillation using the same methods described previously¹³ while the NiCl₂ was used as purchased. Molten salt solutions of three concentrations of Ni²⁺ in ZnCl₂ (0.05, 0.1, and 1.0 wt %) were prepared by adding NiCl₂ into the purified ZnCl₂ in the desired proportions, in quartz test tubes sealed under an inert atmosphere. Each tube was then maintained at 800 °C for 15 min to fuse the components. The salt mixtures were cooled and transferred to an inert glovebox, recovered, and crushed to a fine powder using an agate mortar and pestle. The resultant mixtures were then loaded into capillaries; each was then evacuated to 10^{−3} Torr and flame-sealed for XAS measurements.¹³

A custom-built furnace system¹³ was used at the Inner Shell Spectroscopy (8-ID) beamline of the National Synchrotron Light Source II (NSLS-II) at Brookhaven National Laboratory to mount the quartz capillaries containing the NiCl₂ in ZnCl₂ mixtures. Ni K-edge X-ray absorption spectra were measured in fluorescence geometry. After ensuring temperature homogeneity above the melting point (290 °C), we collected several absorption spectra for each sample at 320 °C. The spectra were collected using 10–20 min of beam exposure, depending on the concentration of Ni²⁺ in the sample. Further details are given below.

X-ray absorption spectra were processed and analyzed using the Athena and Artemis programs from the Demeter package.²³ Linear combination analysis of XANES data was performed with Athena program. Data analysis of the Ni K-edge EXAFS spectra for the 0.05 wt % NiCl₂ sample was performed using Artemis program. Additional details of the data analysis are given in the [Supporting Information](#).

The relative atomic coordinates of the face centered cubic structures of bulk Ni metal were used to generate perfect cuboctahedron nanoclusters composed of 55 and 147 Ni atoms with nearest neighbor distances corresponding to interatomic distances in bulk Ni. The XANES spectra of these Ni nanoclusters were simulated with the FEFF9 code (see the [Supporting Information](#)). The simulated spectra for the two cluster sizes are very similar and the results for the cluster of 55 atoms are considered in the following discussions ([SI Figure 3](#)).

In previous work, neural network-assisted XANES analysis has proven to be an effective tool for structural analysis of monometallic,^{24–27} bimetallic,²⁸ and metal oxide nanoparticles and clusters.²⁹ In this method, a convolutional neural network is trained to “understand” the relationship between the spectral features of an unknown material and its structure through the first nearest-neighboring coordination numbers (CN), utilizing a training set comprised of a large number of labeled spectra for which the relationship is known. Here, the site-specific XANES spectra of different structural models of Ni nanoparticles were simulated with the FEFF9 program; then a convolutional analysis was performed to analyze correlations between the XANES spectra and structural descriptors such as Ni–Ni coordination numbers (CN). More detailed information on the neural network-assisted XANES method is given in the [Supporting Information](#).

The edge-step-normalized XANES spectra at the Ni K-edge for 0.05, 0.1, and 1.0 wt % NiCl₂ in ZnCl₂ measured at 320 °C are presented in Figure 1. Along with distinctive changes in the white line intensity (at ca. 8349 eV) Figure 1a shows a systematic increase in intensity of the mid-edge region that subtly shifts toward lower energies with decreasing Ni²⁺ concentration. Panels b and c of Figure 1 compare the 1.0 wt % sample and the 0.05 wt % sample with room-temperature (RT) absorption coefficients of pure NiCl₂ and Ni metal samples, respectively. These comparisons offer clues about the local site symmetry of the absorbing Ni species in the three different samples. In Figure 1b, the double-peak structure of the white line for the room-temperature NiCl₂ sample is characteristic of an octahedral (O_h) coordination environment around the Ni ions, while the reduced intensity and shape change of the white line region observed at 320 °C for 1.0 wt % Ni in ZnCl₂ is indicative of a structural transformation to a disordered tetrahedral coordination.¹³ In Figure 1c, although there is a qualitative similarity in the spectral features of the 0.05 wt % NiCl₂ in ZnCl₂ sample and bulk Ni that attests to the metallic character of Ni in the salt solution, there are clear discrepancies between the two spectra in the intensity and position of the mid-edge feature as well as smeared oscillations in the EXAFS region for the 0.05 wt % NiCl₂ sample. While the XANES spectrum for the 0.1 wt % NiCl₂ in ZnCl₂ differs from both the less (0.05 wt %) and the more (1.0 wt %) concentrated solutions, multiple isosbestic points are evident in Figure 1a, indicating that the coordination state of Ni in the 0.1 wt % sample can be represented as a mixture of two states, corresponding to those found in the 0.05 and 1.0 wt % samples.

Figure 2 presents a linear combination analysis (LCA) of Ni K-edge XANES spectra for the 0.1 wt % Ni sample at 320 °C

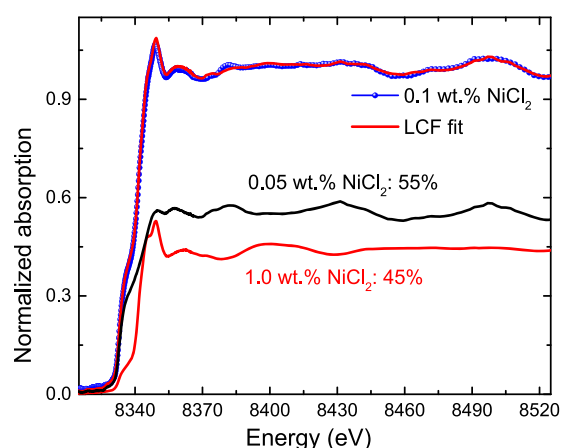


Figure 2. Linear combination analysis of the experimental XANES spectrum recorded at the Ni K-edge of 0.1 wt % NiCl₂ in ZnCl₂ at 320 °C. The fitting was performed using the spectra of 0.05 and 1.0 wt % NiCl₂ in ZnCl₂ at 320 °C as references. Reference spectra are adjusted for better view.

using the 0.05 and 1.0 wt % NiCl₂ spectra as references. Good agreement between the linear combination spectrum and experimental data for 0.1 wt % NiCl₂ confirms the hypothesis above. As a result of the LCA, we conclude that the mole fractions of Ni²⁺ and of Ni⁰ in the 0.1 wt % NiCl₂ sample are, approximately, 0.45 and 0.55, respectively.

We now focus our attention on the metallic phase observed in the 0.05 wt % NiCl₂ sample. The similarity between the 0.05 wt % NiCl₂ and bulk Ni spectra highlighted in Figure 1c offers two distinct possibilities: the X-ray-driven radiolytic reduction produces monometallic Ni nanoparticles, or it leads to the formation of bimetallic Ni (core)–Zn (shell) nanoparticles. In principle, both scenarios are feasible depending on the degree of reduction of nickel compared to the initial concentration of NiCl₂. To differentiate between these possibilities, we conducted *ab initio* simulations of the spectra for the two possible structures and compared them with the simulated XANES spectrum of bulk Ni (SI Figure 1 and inset of Figure 1c). As shown in the inset of Figure 1c, comparison of the Ni K-edge XANES spectra simulated for a representative 55-atom Ni nanoparticle and a Ni foil reproduces the experimentally observed differences between the 0.05 wt % NiCl₂ sample and bulk Ni sample reasonably well. For comparison, we performed simulation of the spectrum for a 147-atom nanoparticle (SI Figure 2), showing similar discrepancies from the spectrum simulated for the bulk metal. Comparison of the simulated XANES spectrum for a bimetallic Ni core–Zn shell nanoparticle reveals significant differences from the bulk Ni theoretical spectrum (SI Figure 1).

Supporting evidence for radiolytic formation of pure Ni nanoparticles in the 0.05 wt % NiCl₂ sample is found by comparing its EXAFS spectrum with those of Ni and Zn foils. Figure 3a demonstrates that the positions of the first nearest neighbor peak of the 0.05 wt % sample and room-temperature metallic Ni are in good agreement and the distance is very different from the corresponding peak for metallic Zn, confirming predominant coordination of Ni atoms are by Ni, not Zn. EXAFS of the 1 wt % sample shows no evidence of metallic Ni at 320 °C, as expected. Figure 3b presents a quantitative analysis of the EXAFS region at the Ni K-edge for the 0.05 wt % NiCl₂ sample at 320 °C and provides insight into the local coordination environment around Ni atoms in the 0.05 wt % sample. (The best fit results are summarized in SI Table 1.) The predicted coordination number is 7.0 ± 1.4 . Assuming a face-centered-cubic cuboctahedral structure,^{30,31} this value is similar to that expected for a 55-atom cluster (first nearest-neighbor coordination number, 7.86³¹) in agreement with the prediction of the XANES simulation (*vide infra*). Assuming a distance between two adjacent Ni atoms of 0.25 nm (SI Table 1), the approximate particle diameter for a 55-atom cuboctahedral nanoparticle model is $4 \times 0.25 \text{ nm} = 1.0 \text{ nm}$.³²

To further validate our EXAFS analysis results, we used neural network-assisted XANES analysis to “invert” the experimental XANES spectrum and extract the Ni–Ni coordination number from the XANES data. Good agreement between the experimental and theoretical (calculated with FEFF9) XANES spectra for the Ni foil are shown in SI Figure 3, validating the use of FEFF9 for generating training sets for neural network training. Theoretical, particle-averaged XANES spectra and experimental XANES spectra (for bulk Ni and 0.05 wt % Ni²⁺ in ZnCl₂) were used to validate the NN performance. Both theoretical and experimental validation results are well aligned on the diagonal in Figure 4, demonstrating the utility of the NN analysis. For the experimental XANES spectra of bulk Ni, a Ni–Ni CN of 12.2 was obtained, which is close to the value of 12 as expected for the face-centered-cubic structure of bulk Ni. For 0.05 wt % NiCl₂ at 320 °C, a Ni–Ni CN of 7.3 was obtained, which is in

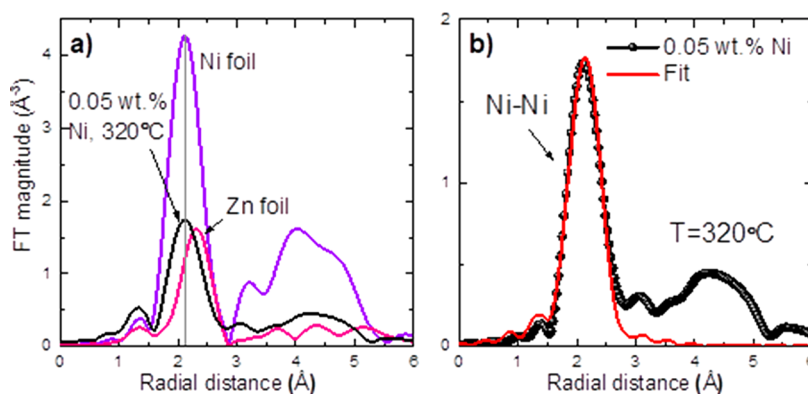


Figure 3. (a) Fourier-transform magnitudes of k^2 -weighted EXAFS spectra for 0.05 wt % NiCl_2 in ZnCl_2 at 320 °C, and Ni and Zn metal foils (RT). (b) Fourier-transform magnitudes of k^2 -weighted data and theoretical fit for Ni K-edge EXAFS spectra for 0.05 wt % NiCl_2 in ZnCl_2 at 320 °C.

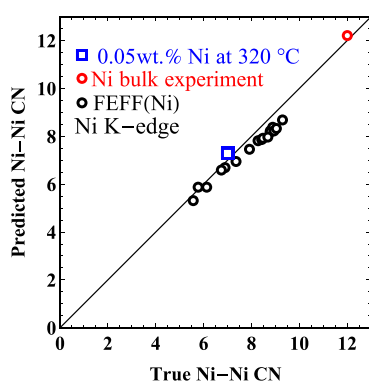


Figure 4. Validation of NN analysis comparing agreement between theoretical particle-averaged and experimental XANES data. Results from the NN-XANES analysis of Ni–Ni coordination numbers (vertical axis) obtained using simulated XANES data for Ni particles with different sizes are compared with the true Ni–Ni coordination number (horizontal axis). The experimental coordination numbers (CN) shown on the x -axis were obtained from the known crystal structures and from EXAFS analysis of bulk Ni^0 and 0.05 wt % NiCl_2 at 320 °C, respectively.

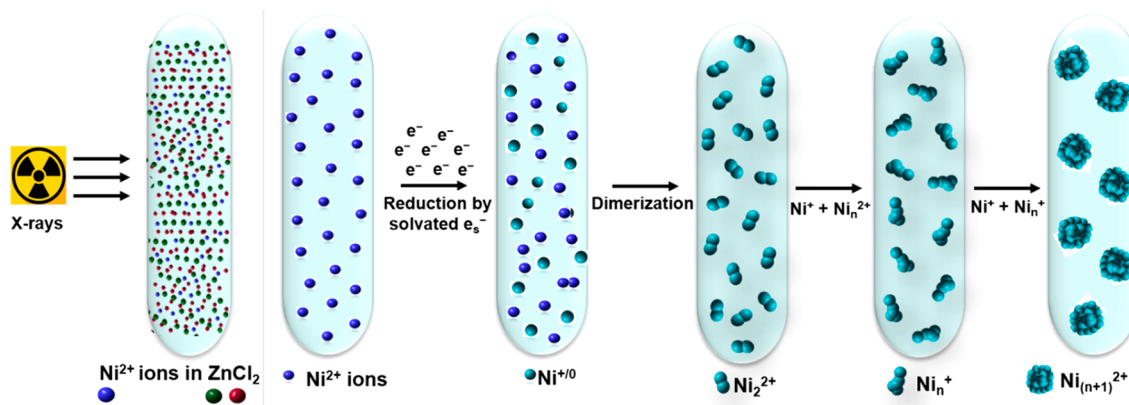
very good agreement with the result of the EXAFS analysis, 7.0.

In summary, analyses of XANES and EXAFS data of 0.05, 0.1, and 1 wt % NiCl_2 in ZnCl_2 at 320 °C show significant reduction of the starting Ni^{2+} and the formation of Ni

nanoparticles when the NiCl_2 content is low. In the lowest concentration solution considered, 0.05 wt % Ni^{2+} in ZnCl_2 , metallic Ni nanoparticles of approximately 1 nm average diameter are produced by radiolysis, while in the highest concentration solution, 1.0 wt % Ni^{2+} in ZnCl_2 , a fluxional combination of distorted four- and five-coordinate Ni^{2+} species are observed.¹³ In the intermediate concentration solution, 0.1 wt % Ni^{2+} in ZnCl_2 , a mixture of the two end states, in the ratio 55% Ni^0 to 45% Ni^{2+} is observed. We hypothesize that formation of Ni metal nanoparticles is due to radiolysis of the sample by the high X-ray dose during the XAS measurements, with solvated electrons generated by X-ray irradiation leading to the reduction of Ni^{2+} ions in the molten zinc chloride. A mechanism of metal nanoparticle formation in molten salt systems is proposed, and the dependence of our observations on NiCl_2 concentration and radiation dose are discussed in the following section.

If radiation from the X-ray beam is responsible for production of Ni metal by the reduction of Ni^{2+} in the samples, the observed proportions of Ni^0 /total Ni calculated by the linear combination analysis above (1.0, 0.55, and ~ 0 for 0.05, 0.1, and 1.0 wt % Ni^{2+} in ZnCl_2 , respectively, SI Table 2) ought to be related to the amount of radiation absorbed by each sample:

Scheme 1. Schematic Showing X-ray Induced Ni Nanoparticle Formation in Molten Zinc Chloride



$$\frac{g_{0.1}}{g_{0.05}} = \frac{C_{0.05} t_{0.1}}{C_{0.1} t_{0.05}} = 0.5 \quad \text{and}$$

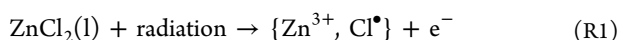
$$\frac{g_{1.0}}{g_{0.05}} = \frac{C_{0.05} t_{1.0}}{C_{1.0} t_{0.05}} = 0.0225 \quad (1)$$

In eq 1, employed to estimate the expected proportions of Ni⁰ in the 0.1 and 1.0 wt % samples relative to the 0.05 wt % sample, the symbols $g_{0.05}$, $g_{0.1}$, and $g_{1.0}$ represent the calculated fractions of Ni⁰/total Ni for each sample and $C_{0.05}$, $C_{0.1}$, and $C_{1.0}$ are the starting concentrations of NiCl₂ in each sample in wt %. As the mounting geometry, beam area (1 × 1 mm²), and beam flux were the same for all three samples, the radiation dose applied to each sample is proportional to its exposure time. The exposure times for the three samples (labeled $t_{0.05}$, $t_{0.1}$, and $t_{1.0}$) were 20, 20, and 9 min, respectively (SI Table 2).

The percentages of Ni⁰ estimated in the three samples using eq 1 are 100:50:2.2. These values are very similar to those (100:55:0) extracted from the XANES data using the linear combination analysis (SI Table 2). Equation 1 implicitly assumes that the 0.05 wt % sample was not irradiated in gross excess of the point of full conversion to Ni⁰. This estimation is also consistent with the lack of observation of Ni⁰ in the 1.0 wt % sample; the calculated value of 2.2% is below the precision limit of the linear combination analysis. As the conversion percentages are consistent between the two approaches, we conclude that our hypothesis, i.e., that X-ray induced radiolytic reduction is predominantly responsible for forming metallic Ni in the samples, is valid.

The mechanistic role of synchrotron X-ray irradiation in the reduction of nickel ions and the formation of metallic Ni nanoparticles is summarized schematically in Scheme 1. The first step involves the radiolysis of the solvent, molten ZnCl₂, by the X-rays producing excess electrons (e⁻) and holes (electron vacancies, i.e., Zn³⁺ and Cl[•], reaction 1). As the yield of ionization approximately follows the wt % of a particular ion, direct ionization of Ni²⁺ is negligible even in the most concentrated solution considered. Any “high oxidation state” Zn³⁺ produced rapidly transfers its hole to a coordinating Cl⁻ (reaction R2), leaving the chlorine atom Cl[•] as the sole primary oxidized species. Recombination of the initially formed excess electron and chlorine atom (reaction R3) competes on the picosecond time scale with formation of the dichlorine radical anion (reaction R4) and capture of the excess electron by Zn²⁺ cation (reaction R5). Zn⁺ and Cl₂^{•-} are the dominant reducing and oxidizing species in this system on the nanosecond and longer time scales. In pure molten ZnCl₂, i.e., without any added NiCl₂, Zn⁺ and Cl₂^{•-} will react, recombining the radiolytically produced excess charges (reaction R6). In addition, two dichlorine radical anions can react with each other, disproportionating into trichloride and chloride anions (reaction R7). Reaction R6 is significantly faster than reaction R7, so reaction R7 is only significant when Cl₂^{•-} is in excess, to wit, when there is some other reaction pathway that removes the reducing species Zn⁺.

Radiolysis



Hole transfer



Fast (ps) recombination



Dimerization



Reduction of Zn²⁺



Diffuse recombination

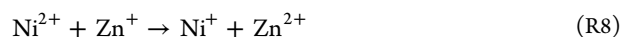


Disproportionation of Cl₂^{•-}



Under the conditions of these experiments, the concentration of Ni²⁺ is much higher (9.7, 19.4, and 194 mM for 0.05, 0.1, and 1 wt %, respectively) than the steady-state concentrations of Zn⁺ and Cl₂^{•-} produced by radiolysis. Therefore, the reduction of Ni²⁺ by Zn⁺ (reaction R8) should proceed quantitatively. The reduced Ni⁺ is subject to oxidation by Cl₂^{•-} (reaction R9) with a rate coefficient that is likely to be similar to reaction R6 and significantly faster than reaction R7 (reactions R6 and R9 are electron transfer reactions with significant driving forces, while reaction R7 is an atom transfer reaction). Most of the radiolytically generated excess charges are annihilated via reaction R9, but a small fraction of Ni⁺ may dimerize to form the seed of a nickel cluster (reaction R10):

Reduction of Ni²⁺



Oxidation of Ni⁺

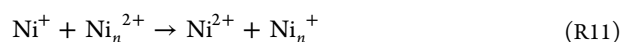


Dimerization of Ni⁺



The seed can grow into a cluster and then a nanoparticle through a combination of electron transfer and metal-ion addition steps (reactions R11 and R12).

Electron transfer



Addition



While reactions R11 and R12 depict the growing cluster alternating between mono- and divalent states, the mechanism would work the same way with neutral and monovalent states, as sometimes postulated for metal cluster growth in aqueous media. However, in a molten salt the formation of a neutral cluster may be less favorable. In either case, the reduction potentials of the Ni_n^{2+/+} and Ni_n^{+ /0} couples increase asymptotically toward their bulk values as n increases.²

As the cluster grows, it is also subject to corrosion by the attack of Cl₂^{•-}, analogous to reaction R9. Overall, the mechanism of Ni nanoparticle formation in molten ZnCl₂ is very inefficient, due to the reactivity of Cl₂^{•-} in reactions R6 and R9. In most work that employs radiolysis for nanoparticle synthesis, a sacrificial reactant is added to remove the oxidizing species, resulting in efficient formation and growth of

nanoparticles.² In this chemical system, reaction R7 is the only alternate path for removing $\text{Cl}_2^{\bullet-}$ without oxidizing a metal ion, by converting $\text{Cl}_2^{\bullet-}$ to less strongly oxidizing Cl_3^- . Reaction R7 is an inner-sphere transfer of a chlorine atom between two anions, and as such it is expected to be slower than the electron transfer processes in reactions R6 and R9. Consequently, radiolytic nanoparticle formation is inefficient in this system due to the higher rates of the oxidative corrosion reactions R6 and R9 outcompeting reaction R7. Thus in these experiments, it required doses of at least 274 kGy to fully reduce the 0.05 wt % sample.

The question remains why the metal nanoparticles observed to form under these conditions in the 0.05 wt % NiCl_2 sample are so small (~ 1 nm). When the radiation dose rate is low, the rate at which the reducing species are generated is slow and nanoparticle formation will take place by diffusion mitigated coalescence and adsorption. In this scenario, the concentration of reduced ions is low so a small number of charged clusters are produced and then reduced *in situ*, leading to the formation of a small number of large nanoparticles, i.e., the final mean nuclearity is high. In contrast, when the radiation dose rate is high, radiolytic reduction produces a high concentration of free atoms. These atoms seed the growth of nanoparticles of smaller size, but higher concentration, than would be found at a lower dose rate. This dose-rate effect can be observed in the final size distribution of the nanoparticles.^{33–36} In our experiments, the very high dose rate favors nucleation rather than growth and the production of a high concentration of small nanoparticles.

In summary, *in situ* X-ray absorption spectroscopy has been utilized for real time characterization of radiolytic nickel metal ion reduction in zinc chloride molten salt solutions, and a mechanism for X-ray induced radiolytic nanoparticle formation and growth in molten salt environments is proposed. We demonstrate that solvated electrons produced by X-ray irradiation of Cl^- ions in ZnCl_2 initiate a complex reaction mechanism that ultimately leads to Ni nanoparticle formation. X-ray absorption spectroscopy is combined with *ab initio* XANES modeling, as well as a neural network analysis of XANES data, to determine the average size and the local structure of the metallic Ni metal formed. The observation and yield of Ni nanoparticle formation is dependent on the irradiation dose and the concentration of Ni^{2+} in the precursor solution: a solution initially with 0.05 wt % Ni^{2+} in ZnCl_2 shows complete conversion of Ni^{2+} to metallic Ni nanoparticles of ~ 1 nm diameter when exposed to a dose of 274 Gy, while a 0.1 wt % solution exposed to the same dose shows only 50% conversion, and the conversion in a 1.0 wt % solution is too small to be measured experimentally.

■ ASSOCIATED CONTENT

SI Supporting Information

The Supporting Information is available free of charge at <https://pubs.acs.org/doi/10.1021/acs.jpcllett.0c03231>.

Schematic XANES simulation by FEFF9 and artificial neural network method for prediction of the structure of the nanoparticles; linear-Combination Analysis of XANES data, EXAFS analysis, and X-ray dose estimation. (PDF)

■ AUTHOR INFORMATION

Corresponding Authors

Simerjeet K. Gill – Nuclear Science and Technology Department, Brookhaven National Laboratory, Upton, New York 11973, United States; orcid.org/0000-0003-4955-4509; Email: gills@bnl.gov

Anatoly I. Frenkel – Department of Materials Science and Chemical Engineering, Stony Brook University, Stony Brook, New York 11794, United States; Chemistry Division, Brookhaven National Laboratory, Upton, New York 11973, United States; orcid.org/0000-0002-5451-1207; Email: frenkel@bnl.gov

Authors

Elaine T. Dias – Nuclear Science and Technology Department, Brookhaven National Laboratory, Upton, New York 11973, United States

Yang Liu – Department of Materials Science and Chemical Engineering, Stony Brook University, Stony Brook, New York 11794, United States

Phillip Halstenberg – Department of Chemistry, University of Tennessee, Knoxville, Tennessee 37996, United States; orcid.org/0000-0002-6030-4503

Sheng Dai – Department of Chemistry, University of Tennessee, Knoxville, Tennessee 37996, United States; Chemical Sciences Division, Oak Ridge National Laboratory, Oak Ridge, Tennessee 37831, United States; orcid.org/0000-0002-8046-3931

Jiahao Huang – Department of Materials Science and Chemical Engineering, Stony Brook University, Stony Brook, New York 11794, United States

Julia Mausz – Ludwig-Maximilians-Universität München, München 80539, Germany

Ruchi Gakhar – Idaho National Laboratory, Idaho Falls, Idaho 83415, United States

William C. Phillips – Idaho National Laboratory, Idaho Falls, Idaho 83415, United States

Shannon Mahurin – Chemical Sciences Division, Oak Ridge National Laboratory, Oak Ridge, Tennessee 37831, United States; orcid.org/0000-0003-3792-1631

Simon M. Pimblott – Idaho National Laboratory, Idaho Falls, Idaho 83415, United States; orcid.org/0000-0001-9169-3030

James F. Wishart – Chemistry Division, Brookhaven National Laboratory, Upton, New York 11973, United States; orcid.org/0000-0002-0488-7636

Complete contact information is available at: <https://pubs.acs.org/doi/10.1021/acs.jpcllett.0c03231>

Notes

The authors declare no competing financial interest.

■ ACKNOWLEDGMENTS

This work was supported as part of the Molten Salts in Extreme Environments Energy Frontier Research Center, funded by the U.S. Department of Energy Office of Science. BNL, INL, and ORNL are operated under DOE contracts DE-SC0012704, DE-AC07-05ID14517, and DE-AC05-00OR22725, respectively. This research used resources of the ISS (8-ID) beamline at the National Synchrotron Light Source II operated by BNL under Contract No. DE-SC0012704, a U.S. Department of Energy (DOE) Office of

Science User Facility. The FEFF simulations used resources of the Center for Functional Nanomaterials, which is a U.S. DOE Office of Science Facility, and the Scientific Data and Computing Center, a component of the Computational Science Initiative, at BNL under Contract No. DE-SC0012704. The authors thank Drs. Eli Stavitski and Mehmet Topsakal for help with XAS data collection, and Mr. Bobby Layne for help with the design and operation of the *in situ* XAS furnace.

REFERENCES

- (1) Reddy, R. G. Molten Salts: Thermal Energy Storage and Heat Transfer Media. *J. Phase Equilib. Diffus.* **2011**, *32*, 269.
- (2) Belloni, J.; Marignier, J. L.; Mostafavi, M. Mechanisms of metal nanoparticles nucleation and growth studied by radiolysis. *Radiat. Phys. Chem.* **2020**, *169*, 107952.
- (3) Ding, K.; Miao, Z.; Liu, Z.; Zhang, Z.; Han, B.; An, G.; Miao, S.; Xie, Y. Facile Synthesis of High Quality TiO₂ Nanocrystals in Ionic Liquid via a Microwave-Assisted Process. *J. Am. Chem. Soc.* **2007**, *129*, 6362–6363.
- (4) Minamimoto, H.; Irie, H.; Uematsu, T.; Tsuda, T.; Imanishi, A.; Seki, S.; Kuwabata, S. Fine Patterning of Silver Metal by Electron Beam Irradiation onto Room-temperature Ionic Liquid. *Chem. Lett.* **2015**, *44*, 312–314.
- (5) Tsuda, T.; Sakamoto, T.; Nishimura, Y.; Seino, S.; Imanishi, A.; Kuwabata, S. Various metal nanoparticles produced by accelerated electron beam irradiation of room-temperature ionic liquid. *Chem. Commun.* **2012**, *48*, 1925–1927.
- (6) Baba, K.; Kaneko, T.; Hatakeyama, R. Efficient Synthesis of Gold Nanoparticles Using Ion Irradiation in Gas-Liquid Interfacial Plasmas. *Appl. Phys. Express* **2009**, *2*, 035006.
- (7) Čubová, K.; Čuba, V. Synthesis of inorganic nanoparticles by ionizing radiation - a review. *Radiat. Phys. Chem.* **2020**, *169*, 108774.
- (8) Sun, W.; Li, X.; Qin, P.; Jiao, K. Electrodeposition of Co Nanoparticles on the Carbon Ionic Liquid Electrode as a Platform for Myoglobin Electrochemical Biosensor. *J. Phys. Chem. C* **2009**, *113*, 11294–11300.
- (9) Höfft, O.; Endres, F. Plasma electrochemistry in ionic liquids: an alternative route to generate nanoparticles. *Phys. Chem. Chem. Phys.* **2011**, *13*, 13472–13478.
- (10) Zhang, H.; Dasbiswas, K.; Ludwig, N. B.; Han, G.; Lee, B.; Vaikuntanathan, S.; Talapin, D. V. Stable colloids in molten inorganic salts. *Nature* **2017**, *542*, 328–331.
- (11) Kamysbayev, V.; Srivastava, V.; Ludwig, N. B.; Borkiewicz, O. J.; Zhang, H.; Ilavsky, J.; Lee, B.; Chapman, K. W.; Vaikuntanathan, S.; Talapin, D. V. Nanocrystals in Molten Salts and Ionic Liquids: Experimental Observation of Ionic Correlations Extending beyond the Debye Length. *ACS Nano* **2019**, *13*, 5760–5770.
- (12) Muñoz-Sánchez, B.; Nieto-Maestre, J.; Iparraguirre-Torres, I.; García-Romero, A.; Sala-Lizarraga, J. M. Molten salt-based nanofluids as efficient heat transfer and storage materials at high temperatures. An overview of the literature. *Renewable Sustainable Energy Rev.* **2018**, *82*, 3924–3945.
- (13) Gill, S. K.; Huang, J.; Mausz, J.; Gakhar, R.; Roy, S.; Vila, F.; Topsakal, M.; Phillips, W. C.; Layne, B.; Mahurin, S.; Halstenberg, P.; Dai, S.; Wishart, J. F.; Bryantsev, V. S.; Frenkel, A. I. Connections between the Speciation and Solubility of Ni(II) and Co(II) in Molten ZnCl₂. *J. Phys. Chem. B* **2020**, *124*, 1253–1258.
- (14) Hardacre, C. APPLICATION OF EXAFS TO MOLTEN SALTS AND IONIC LIQUID TECHNOLOGY. *Annu. Rev. Mater. Res.* **2005**, *35*, 29–49.
- (15) Hefeng, L.; Kunquan, L.; Zhonghua, W.; Jun, D. EXAFS studies of molten ZnCl₂, RbCl and Rb₂ZnCl₄. *J. Phys.: Condens. Matter* **1994**, *6*, 3629–3640.
- (16) Okamoto, Y.; Akabori, M.; Motohashi, H.; Itoh, A.; Ogawa, T. High-temperature XAFS measurement of molten salt systems. *Nucl. Instrum. Methods Phys. Res., Sect. A* **2002**, *487*, 605–611.
- (17) Smith, A. L.; Verleg, M. N.; Vlieland, J.; de Haas, D.; Ocadiz-Flores, J. A.; Martin, P.; Rothe, J.; Dardenne, K.; Salanne, M.; Gheribi, A. E.; Capelli, E.; van Eijck, L.; Konings, R. J. M. In situ high-temperature EXAFS measurements on radioactive and air-sensitive molten salt materials. *J. Synchrotron Radiat.* **2019**, *26*, 124–136.
- (18) Ma, J.; Zou, Y.; Jiang, Z.; Huang, W.; Li, J.; Wu, G.; Huang, Y.; Xu, H. An in situ XAFS study—the formation mechanism of gold nanoparticles from X-ray-irradiated ionic liquid. *Phys. Chem. Chem. Phys.* **2013**, *15*, 11904–11908.
- (19) Fong, Y.-Y.; Visser, B. R.; Gascooke, J. R.; Cowie, B. C. C.; Thomsen, L.; Metha, G. F.; Buntine, M. A.; Harris, H. H. Photoreduction Kinetics of Sodium Tetrachloroaurate under Synchrotron Soft X-ray Exposure. *Langmuir* **2011**, *27*, 8099–8104.
- (20) Ohkubo, Y.; Nakagawa, T.; Seino, S.; Kugai, J.; Yamamoto, T. A.; Nitani, H.; Niwa, Y. X-ray-induced reduction of Au ions in an aqueous solution in the presence of support materials and in situ time-resolved XANES measurements. *J. Synchrotron Radiat.* **2014**, *21*, 1148–1152.
- (21) Bharti, A.; Bhardwaj, R.; Agrawal, A. K.; Goyal, N.; Gautam, S. Monochromatic X-Ray Induced Novel Synthesis of Plasmonic Nanostructure for Photovoltaic Application. *Sci. Rep.* **2016**, *6*, 22394.
- (22) Grand, J.; Ferreira, S. R.; de Waele, V.; Mintova, S.; Nenoff, T. M. Nanoparticle Alloy Formation by Radiolysis. *J. Phys. Chem. C* **2018**, *122*, 12573–12588.
- (23) Ravel, B.; Newville, M. ATHENA, ARTEMIS, HEPHAESTUS: data analysis for X-ray absorption spectroscopy using IFEFFIT. *J. Synchrotron Radiat.* **2005**, *12*, 537–541.
- (24) Timoshenko, J.; Lu, D.; Lin, Y.; Frenkel, A. I. Supervised machine-learning-based determination of three-dimensional structure of metallic nanoparticles. *J. Phys. Chem. Lett.* **2017**, *8*, 5091–5098.
- (25) Timoshenko, J.; Halder, A.; Yang, B.; Seifert, S.; Pellin, M. J.; Vajda, S.; Frenkel, A. I. Subnanometer Substructures in Nano-assemblies Formed from Clusters under a Reactive Atmosphere Revealed Using Machine Learning. *J. Phys. Chem. C* **2018**, *122*, 21686–21693.
- (26) Reese, S.; Kononov, A.; Timoshenko, J.; Frenkel, A. I.; Hövel, H. Cluster Assemblies Produced by Aggregation of Preformed Ag Clusters in Ionic Liquids. *Langmuir* **2018**, *34*, 4811–4819.
- (27) Timoshenko, J.; Frenkel, A. I. “Inverting” X-ray Absorption Spectra of Catalysts by Machine Learning in Search for Activity Descriptors. *ACS Catal.* **2019**, *9*, 10192–10211.
- (28) Marcella, N.; Liu, Y.; Timoshenko, J.; Guan, E.; Luneau, M.; Shirman, T.; Plonka, A. M.; van der Hoeven, J.; Aizenberg, J.; Friend, C.; Frenkel, A. I. Neural network assisted analysis of bimetallic nanocatalysts using X-ray absorption near edge structure spectroscopy. *Phys. Chem. Chem. Phys.* **2020**, *22*, 18902–18910.
- (29) Liu, Y.; Marcella, N.; Timoshenko, J.; Halder, A.; Yang, B.; Kolipaka, L.; Pellin, M. J.; Seifert, S.; Vajda, S.; Liu, P.; Frenkel, A. I. Mapping XANES spectra on structural descriptors of copper oxide clusters using supervised machine learning. *J. Chem. Phys.* **2019**, *151*, 164201.
- (30) Frenkel, A. I.; Hills, C. W.; Nuzzo, R. G. A View from the Inside: Complexity in the Atomic Scale Ordering of Supported Metal Nanoparticles. *J. Phys. Chem. B* **2001**, *105*, 12689–12703.
- (31) Glasner, D.; Frenkel, A. I. Geometrical Characteristics of Regular Polyhedra: Application to EXAFS Studies of Nanoclusters. *AIP Conf. Proc.* **2006**, *882*, 746–748.
- (32) Li, Y.; Zakharov, D.; Zhao, S.; Tappero, R.; Jung, U.; Elsen, A.; Baumann, P.; Nuzzo, R. G.; Stach, E. A.; Frenkel, A. I. Complex structural dynamics of nanocatalysts revealed in Operando conditions by correlated imaging and spectroscopy probes. *Nat. Commun.* **2015**, *6*, 7583.
- (33) Treguer, M.; de Cointet, C.; Remita, H.; Khatouri, J.; Mostafavi, M.; Amblard, J.; Belloni, J.; de Keyser, R. Dose Rate Effects on Radiolytic Synthesis of Gold-Silver Bimetallic Clusters in Solution. *J. Phys. Chem. B* **1998**, *102*, 4310–4321.
- (34) Flores-Rojas, G. G.; López-Saucedo, F.; Bucio, E. Gamma-irradiation applied in the synthesis of metallic and organic nanoparticles: A short review. *Radiat. Phys. Chem.* **2020**, *169*, 107962.

(35) Ghoreishian, S. M.; Kang, S.-M.; Seeta Rama Raju, G.; Norouzi, M.; Jang, S.-C.; Yun, H. J.; Lim, S. T.; Han, Y.-K.; Roh, C.; Huh, Y. S. γ -Radiolysis as a highly efficient green approach to the synthesis of metal nanoclusters: A review of mechanisms and applications. *Chem. Eng. J.* **2019**, *360*, 1390–1406.

(36) Mostafavi, M.; Liu, Y.-P.; Pascal, P.; Belloni, J. Dose rate effect on size of CdS clusters induced by irradiation. *Radiat. Phys. Chem.* **2000**, *59*, 49–59.